Chemical Engineering Journal 381 (2020) 122576

Contents lists available at ScienceDirect

Chemical Engineering Journal

journal homepage: www.elsevier.com/locate/cej

Cobalt nanoparticle with tunable size supported on nitrogen-deficient graphitic carbon nitride for efficient visible light driven H_2 evolution reaction

Dan Zhang[a,1], Lu Peng[b,1], Ke Liu[a], Hermenegildo Garcia[b,*], Chuanzhi Sun[a,*], Lin Dong[c]

[a] College of Chemistry, Chemical Engineering and Materials Science, Shandong Provincial Key Laboratory of Clean Production of Fine Chemicals, Institute of Materials and Clean Energy, Shandong Normal University, Jinan 250014, PR China

[b] Instituto Universitario de Tecnología Química, Consejo Superior de Investigaciones Científicas-Universitat Politécnica de Valencia, Universitat Politecnica de Valencia, Av. De los Naranjos s/n, 46022 Valencia, Spain

[c] School of the Environment, Jiangsu Key Laboratory of Vehicle Emissions Control, Nanjing University, Nanjing 210093, PR China

HIGHLIGHTS

- The size of cobalt nanoparticle can be successfully tuned.
- Nitrogen vacancies is generated by metallic Co catalyzed hydrogenation.
- Generation of H· radical is sped up by Co nanoparticles as co-catalysts.

GRAPHICAL ABSTRACT

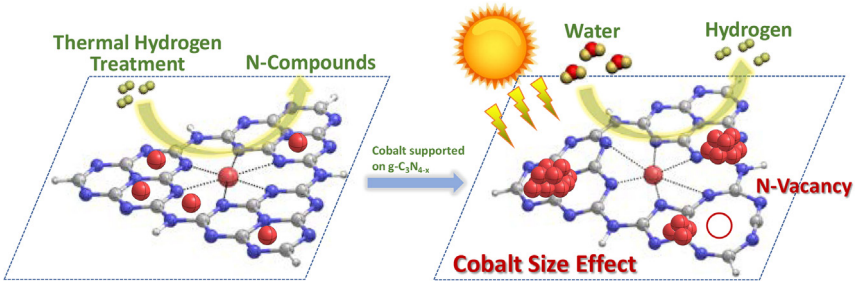

ARTICLE INFO

Keywords:
H_2 evolution
Visible light driven photocatalysis
Metallic cobalt cocatalyst
Nitrogen deficient graphitic carbon nitride

ABSTRACT

Cobalt nanoparticle with tunable size supported on nitrogen-deficient graphitic carbon nitride (Co/g-C_3N_{4-x}) was successfully realized in this work. The formation of metallic Co nanoparticle and N-deficiency generation were performed by H_2 reduction in simple one step. The size of the Co nanoparticle was tuned by changing the reduction temperature and the amount of cobalt salt precursor. The Co/g-C_3N_{4-x} catalyst with the cobalt nanoparticle size in the range of (3.6 ± 2.2) nm exhibited the best H_2-production rate of 750.2 μmol g^{-1} h^{-1} under the visible light (λ > 420 nm), which is 101.4 times higher than pure g-C_3N_4. In addition, some Co atoms were embedded in the lattice structure of g-C_3N_4. According to the experimental and DFT computational results, the band gap of the photocatalyst was narrowed by both Co doping into the g-C_3N_{4-x} lattice and the generation of N deficiency. The metallic Co loaded on g-C_3N_{4-x} surface promoted the electron transfer rate and electron-hole separation efficiency of the photocatalyst. EPR spectroscopy using a trapping agent had been able to determine that H· was formed as intermediate in H_2 generation and its concentration increased due to the presence of Co nanoparticles as co-catalysts. Our work provided a simple method for producing large scale photocatalyst with high efficient H_2 evolution.

* Corresponding authors.
E-mail addresses: hgarcia@qim.upv.es (H. Garcia), suncz@sdnu.edu.cn (C. Sun).
[1] D. Zhang and L. Peng contributed equally to this work.

https://doi.org/10.1016/j.cej.2019.122576
Received 16 May 2019; Received in revised form 20 August 2019; Accepted 21 August 2019
Available online 24 August 2019
1385-8947/

1. Introduction

Due to the rapid consumption of fossil fuels and the increasingly serious environmental pollution, the development of clean renewable energy—hydrogen energy has attracted wide attention [1,2]. The use of abundant sunlight and water resources on the earth to obtain H_2 by photocatalytic technology is considered a promising method to convert sunlight into fuels [3]. Since Honda and Fujishima first report the photocatalytic decomposition of water on TiO_2 in 1972 [4], many semiconducting materials have been intensively studied and applied to water splitting [5–7]. Although many achievements have been made, most of the currently used photocatalysts still have disadvantages such as wide band gap, low visible light efficiency, instability and high price, which hinder the practical application of photocatalytic technology [8,9]. Therefore, it is still necessary to prepare an environment-friendly photocatalyst with good visible light response, high efficiency and low cost.

In recent years, due to the suitable band gap (E_g = 2.7 eV), good stability, lack of toxicity and low cost, graphitic carbon nitride (g-C_3N_4) has become a promising photocatalyst [10–12]. However, g-C_3N_4 shows some disadvantages, such as high recombination rate of photogenerated electron-hole pairs, low utilization of visible light and low conductivity, resulting in an unsatisfactory photocatalytic efficiency [13]. In order to improve the photocatalytic activity of g-C_3N_4 based materials, numerous methods have been performed, such as element doping [14], enhancement of specific surface area [15], supramolecular preorganization of monomers to obtain organized g-C_3N_4 architectures [16,17], construction of heterojunctions with other semiconductors, and among others [18–21]. Loading the co-catalyst on the surface of g-C_3N_4 is an effective way to improve the performance of the photocatalyst by promoting an effective separation of photogenerated electron-hole pairs and facilitating gas evolution. Precious metals supported on the surface such as platinum (Pt) [22], palladium (Pd) [23], gold (Au) [24] and silver (Ag) [25] are common cocatalysts of g-C_3N_4. However, precious metals are expensive and scarce, so the development of inexpensive, highly efficient cocatalysts is advantageous for the large-scale application of photocatalytic water splitting [26]. Recently, cobalt-based catalysts, including CoO [27], $Co(OH)_2$ [28], CoP [29] and so on, have attracted much attention for their excellent performance in photocatalytic decomposition of water. These cobalt-based semiconductors can usually form p-n heterojunction with g-C_3N_4, and then, an internal electric field exists at the interface, which can promote the separation of photogenerated electron-hole pairs, leading to an improved photocatalytic performance [30]. However, it is challengeable to further improve the photocatalytic activity of the p-n heterojunction cobalt-based catalyst. As reported in recent studies [31,32], metallic Co can replace precious metals to achieve the purpose of rapid separation of photogenerated electron-hole pairs improving the photocatalysis process. Various preparation methods have been explored to prepare Co/g-C_3N_4 catalyst to achieve the high photocatalytic activity. Chen et al. [31] loaded the metal cobalt on the surface of the CdS by in-situ photodeposition. In this study, it was shown that the loading of cobalt particles can not only effectively promote the separation of CdS photogenerated electron-hole pairs, but also reduce the overpotential of hydrogen evolution and enhance the photocatalytic activity of the splitting water. Dong et al. [32] explored the key factors for photodeposition of metallic cobalt. This study concluded that metal cobalt particles can be accurately deposited at the g-C_3N_4 electron outlet points by selecting suitable complexing ligands and sacrificial agents, as well as adjusting the illumination time. High efficiency photocatalyst using metallic cobalt as the cocatalyst was obtained.

In this work, high efficiency Co/g-C_3N_4 photocatalysts have been prepared by first obtaining a CoO/g-C_3N_4 material by calcination under argon atmosphere. Then, metallic cobalt nanoparticles supported on g-C_3N_4 were owned by reducing the CoO/g-C_3N_4 precursor in the Ar-H_2 mixed gas. One of the main advantage of our method is that the size of the cobalt nanoparticles can be tuned by changing the amounts of Co $(Ac)_2$ precursor and the reducing temperature, which further influence the activity of catalyst. In addition, generation of N vacancies resulting in the N-deficient graphitic carbon nitride (g-C_3N_{4-x}) occurs simultaneously during the reducing process. The photocatalytic activity of the series of Co/g-C_3N_{4-x} was much higher than that of CoO/g-C_3N_4 and g-C_3N_4 under visible light ($\lambda > 420$ nm). The optimal Co/g-C_3N_{4-x} catalyst showed a high H_2 evolution rate of 750.2 μmol h^{-1} g^{-1}, which is 101.4 times higher than pure g-C_3N_4 and 18.0 times higher than CoO/g-C_3N_4 catalyst under the same conditions. The effect of cobalt doping into g-C_3N_4 lattice and the N deficiency on the light absorption was explored. The role of metal cobalt, the size-dependent effect of cobalt cluster, and the effect of N deficiency on the H_2 evolution rate in photocatalytic reactions has been investigated. Finally, the mechanism of photocatalytic hydrogen evolution was also discussed.

2. Experimental section

2.1. Photocatalysts preparation

The samples were prepared by the thermal condensation method. In a typical process, 10 g of melamine with different amounts of cobalt (II) acetate tetrahydrate were dispersed and dissolved in 60 mL of ethylene glycol, and the mixture was stirred for 30 min under N_2 flow. Subsequently, the mixture was gradually heated to 160 °C, and then 200 mL of 0.2 M aqueous Na_2CO_3 solution was added to the above solution. The slurry was further aged for 1 h with vigorous stirring in N_2 atmosphere. After that, the solid was filtered and washed with distilled water, and dried under vacuum at 50 °C overnight. Finally, the powder was put in a porcelain boat and calcined at 550 °C for 4 h with a heating rate of 5 °C min^{-1} under Ar flow in the tube furnace. The obtained composite samples were CoO/g-C_3N_4 (Fig. S2 shows the XPS of the CoO/ g-C_3N_4 sample, indicating the +2 valence state of Co). The different masses of added cobalt (II) acetate tetrahydrate were 0.01 g, 0.05 g, 0.1 g, 0.15 g and 0.2 g, respectively. They were correspondingly labeled as 0.01CoO/CN, 0.05CoO/CN, 0.1CoO/CN, 0.15CoO/CN and 0.2CoO/CN. Pure g-C_3N_4 was obtained by a similar method without addition of cobalt (II) acetate tetrahydrate and aqueous Na_2CO_3 solution, and it was labeled as CN.

The above obtained samples were placed in a quartz tube and heated in an Ar/H_2 mixed gas atmosphere with a temperature increase rate of 10 °C min^{-1} to 400 °C for 2 h in a micro reactor apparatus. The resulting samples were ground to fine powder, which were labeled as Co/CN. The catalysts with different Co contents were denoted as 0.01Co/CN, 0.05Co/CN, 0.1Co/CN, 0.15Co/CN and 0.2Co/CN.

2.2. Characterization

X-ray diffraction (XRD) patterns of the samples were recorded on a Philips X' pert Pro diffractometer with Cu Kα radiation (λ = 0.15418 nm). Fourier transformed infrared (FTIR) spectra was recorded on a Nicolet IS50 FT-IR spectrometer. The Brunauer-Emmett-Teller (BET) specific surface areas were measured using the Micromeritics ASAP-2020 apparatus. A JEOL 2100 F microscope operating at an acceleration voltage of 200 kV was used in the scanning-transmission mode (STEM). STEM images were collected using a High Angle Annular Dark Field detector (HAADF). The high-resolution transmission electron micrographs (HRTEM) of the samples were obtained using a JEM-2100 transmission electron microscope at an acceleration voltage of 200 kV. Inductively coupled plasma-optical emission spectrometry (ICP-OES) was performed on Thermo Scientific iCAP 7000 apparatus to determine the actual concentration of the elements in the samples. The Escalab 250 Xi (Thermo Scientific) X-ray photoelectron spectrometer with an Al-Kα X-ray ($h\nu$ = 1486.6 eV) was used to perform the X-ray photoelectron spectroscopy (XPS) analysis. The binding energy values obtained in the XPS analysis were corrected by

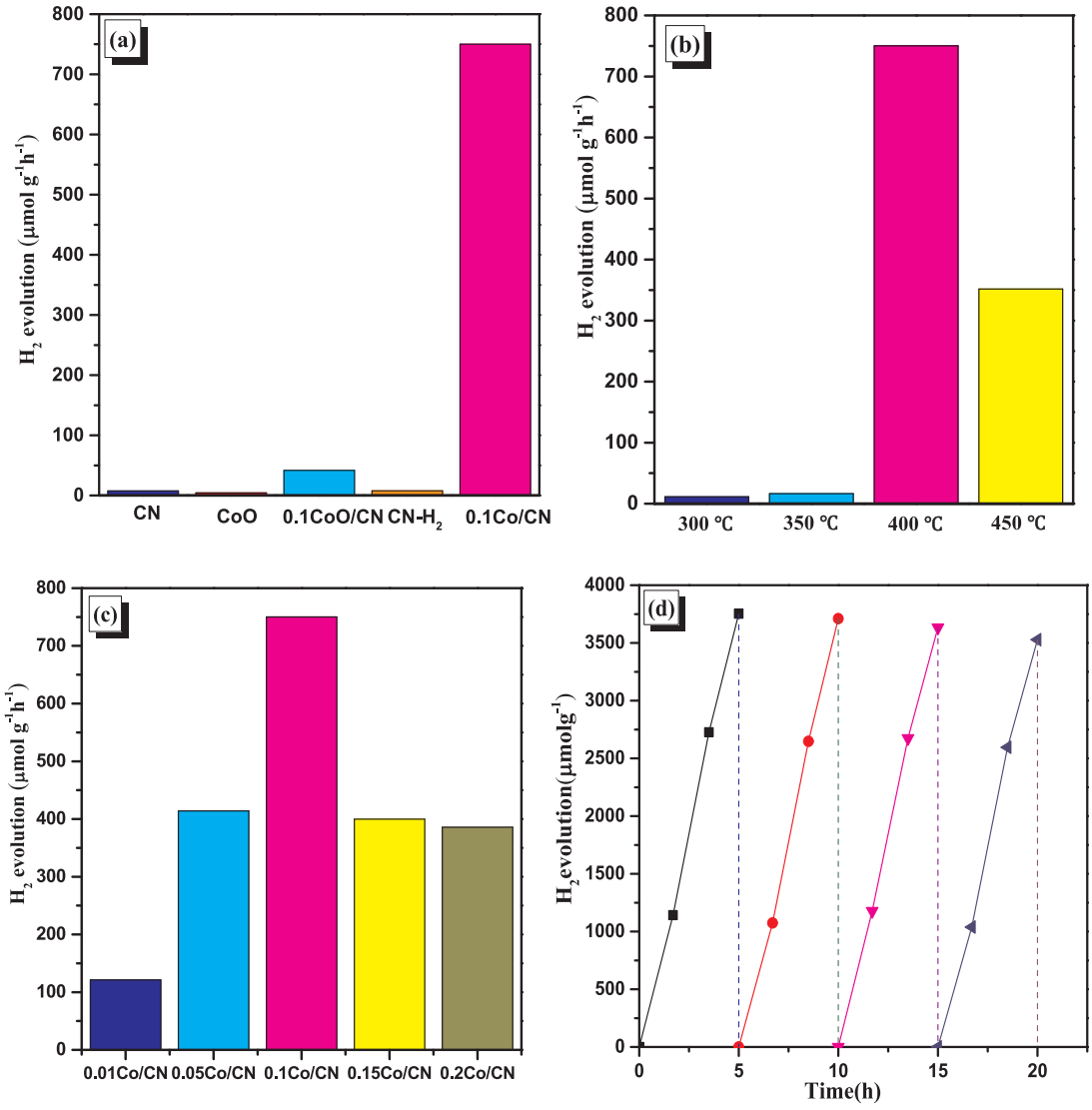

Fig. 1. Photocatalytic H_2 production of (a) CN, CoO, 0.1CoO/CN, CN-H_2 and 0.1Co/CN, (b) photocatalyst 0.1Co/CN obtained by H_2 pretreating at different temperatures, (c) photocatalysts 0.01Co/CN, 0.05Co/CN, 0.1Co/CN, 0.15Co/CN and 0.2Co/CN and (d) 20 h on 0.1Co/CN photocatalyst with evacuation every 5 h. Reaction conditions: 0.1 g photocatalyst, 160 mL H_2O, 40 mL TEOA, 300 W Xe lamp equipped with a cut-off filter at 420 nm.

the C1s peak of 284.6 eV. UV–vis absorption spectra were measured by a UV–visible spectrometer (X-3, YuanXi Instruments). Photoluminescence (PL) spectra was recorded using the FLS-980 Edinburgh Fluorescence Spectrophotometer. Transient photocurrent response, electrochemical impedance spectroscopy (EIS) spectra, and Mott-Schottky (M-S) curves were measured on a CHI-660C electrochemical workstation with a standard three-electrode system. The three-electrode configuration includes a working electrode, a platinum plate as a counter electrode, and Ag/AgCl (saturated KCl) as a reference electrode. The light source was the 300 W xenon lamp with a 420 nm cut-off filter and the electrolyte solution was the 0.1 M Na_2SO_4 solution. Transient photocurrent response and EIS were measured at 0.5 V (vs. Ag/AgCl). The working electrodes were prepared by dispersing 2 mg sample to 2 mL ethanol. Then, 10 μL of 0.25% Nafion was added, followed by sonication for 30 min to obtain a slurry. The suspension was dropped onto a conductive glass (FTO) sheet (1 cm × 2 cm) and dried in an oven at 100 °C for 10 h. The polarization potential range of the Mott-Schottky (M-S) analysis test was −1.5 V to 1 V (vs. Ag/AgCl). The M-S curves at different alternating current potential frequencies were recorded at frequencies of 1 KHz, 1.5 KHz, 2.0 KHz, and 2.5 KHz. Electron paramagnetic resonance (EPR) signals were recorded on a Bruker A300-10/12/S-LC spectrometer. The 2-methyl-N-(4-pyridinylmethylene)-2-propanamine N, N'-dioxide (POBN) was used as a trapping agent.

2.3. DFT calculations

The B3LYP density functional theory was employed to optimize the geometry of models using Gaussion 09 package. For the C, N and H atoms, the standard 6-31G(d) basis set was used, and the effective core potentials of Hay and Wadt combined with double-ζ valence basis sets (LanL2DZ) were used for Co atom. The models of CN were built using three melons with truncated structure, and the H atoms were used on C/N atoms to eliminate boundary influence.

2.4. Photocatalytic tests

Photocatalytic hydrogen generation was carried out in a quartz flask using a 300 W xenon lamp with a 420 nm cut-off filter as the light source. 100 mg of the photocatalyst was dispersed by magnetic stirring into an aqueous solution composed of 160 mL water and 40 mL triethanolamine. Then, before the irradiation experiment, the system was evacuated with a vacuum pump to remove air. The hydrogen production was analyzed by gas chromatography (GC-7900, TCD, Ar as the

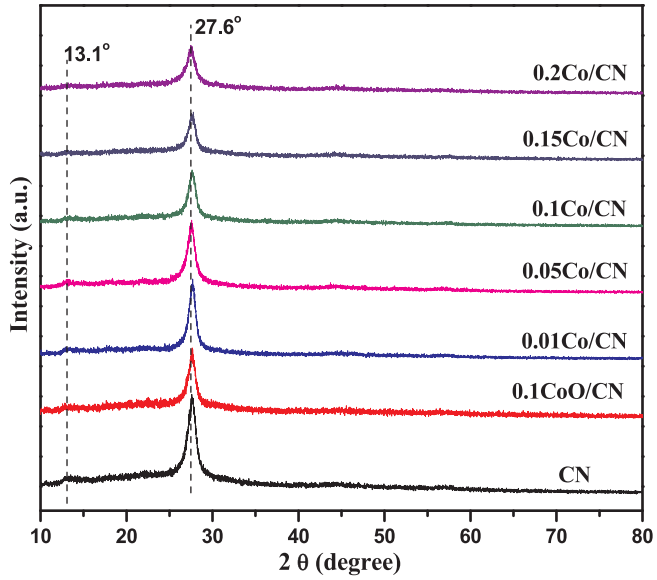

Fig. 2. XRD patterns of CN, 0.1CoO/CN and Co/CN samples with different Co contents.

carrier gas, and 5 Å molecular sieve column).

The external quantum efficiency (EQE) was measured at 405 nm, 420 nm, 450 nm and 500 nm monochromatic wavelength which were obtained by the 300 W Xe lamp with a monochromator. The output intensities were determined by a NOVA II laser power meter (Ophir Photonics). The distance between the light source and the catalytic reaction device is 5 cm. The EQE was calculated through the following Eq. (1)

$$\mathrm{EQE}(100\%) = \frac{\text{number of reacted electrons}}{\text{number of incident photons}} \times 100\% = \frac{\text{number of evolved hydrogen molecules} \times 2}{\text{number of incident photons}} \times 100\% \quad (1)$$

3. Results and discussion

3.1. Photocatalytic activity for H_2 evolution of samples

The H_2 production rates of CN, CoO/CN and Co/CN photocatalysts were tested under visible light irradiation ($\lambda > 420$ nm). Without visible-light irradiation or photocatalyst, no significant hydrogen production was detected for any of the samples, which implied that hydrogen was produced by photocatalysis. Fig. 1 shows photocatalytic H_2 production rates of the different catalysts under study. The H_2 production rate of pure CN is very low (7.4 μmol h^{-1} g^{-1}) due to the rapid recombination of photoexcited electrons of CN [33,34], and the H_2 production rate of pure CoO is also very low (4.3 μmol h^{-1} g^{-1}), as shown in Fig. 1(a). After cobalt species were introduced to CN, the photocatalytic hydrogen production rate is enhanced. As can be seen, the hydrogen production rate of 0.1CoO/CN is 41.8 μmol h^{-1} g^{-1}, which is 5.6 times higher than that of pure CN. After the catalyst is pretreated by H_2, the catalytic activity is increased significantly, and the 0.1Co/CN catalyst shows a high H_2 evolution rate of 750.2 μmol h^{-1} g^{-1}, which is 101.4 times higher than pure CN and 18.0 times higher than 0.1CoO/CN catalyst. The activity of pure CN pretreated with H_2 (denoted as CN-H_2) was tested for comparison. However, its H_2 evolution rate was only 7.8 μmol h^{-1} g^{-1}, which implies the important role of cobalt species. In addition, Fig. S1 shows that the photocatalytic activity of 0.1Co/CN is slightly lower than the activity of 0.5 wt% Pt/CN (907.7 μmol h^{-1} g^{-1}) catalyst. The influence of H_2-pretreated temperature on the activity of Co/CN catalyst was firstly considered. As shown in Fig. 1 (b), the catalysts pretreated at 400 °C show the highest photocatalytic H_2 production rate. Secondly, the effect of cobalt loading on the photocatalytic activity of Co/CN catalysts was investigated. As shown in Fig. 1 (c), with the increase of cobalt content, the photocatalytic H_2 production rate first increases and then decreases, when the cobalt (II) acetate tetrahydrate precursor used is higher than 0.1 g. Therefore, excessive amounts of Co causes a decrease of photocatalytic H_2 production. The activity of 0.1Co/CN under visible-light was also compared with that of other systems based on cobalt species supported on g-C_3N_4 and summarized in Table S1. As can be seen here, the 0.1Co/CN catalyst shows closely or better activity than the other catalysts. Form the above results, it can be concluded that H_2 pretreating on CoO/CN catalyst is a very effective method to obtain high active Co/CN catalysts.

In addition, a recycling study was carried out in order to investigate the stability of the Co/CN composite photocatalyst. As shown in Fig. 1(d), the photocatalyst produced by H_2-pretreating exhibits good stability in the photocatalytic H_2 production reaction process with only a slight decrease in the hydrogen production rate after four cycles. The external quantum efficiency (EQE) of 0.1Co/CN sample upon monochromatic light irradiation is shown in Table S2. It is worth noting that the 0.1Co/CN photocatalyst shows a notable quantum efficiency when the wavelength is higher than 450 nm. As can be seen, the EQE was calculated to be 1.93% and 1.22% at 450 nm and 500 nm, respectively.

3.2. Structure and composition of CN, CoO/CN and Co/CN samples

The XRD patterns of different photocatalysts were recorded to study the phase structure and the dispersed states of cobalt species for different samples. Fig. 2(a) shows XRD patterns of pure CN, 0.1CoO/CN and Co/CN samples. Pure CN has two distinct characteristic peaks at 27.6° and 13.1°, representing the (0 0 2) and (1 0 0) diffraction layer, respectively [35,36]. The strong peak at 27.6° corresponds to the interlayer deposition of the conjugated aromatic system. The weak peak at 13.1° corresponds to the in-plane structural packing motif [11]. For the 0.1CoO/CN and all Co/CN composites, only the diffraction peaks of CN can be observed and no diffraction peaks of CoO or metallic cobalt appear, indicating that the cobalt species are highly dispersed or present as small nanoparticles. In addition, it can be observed that the peak intensity at 27.6° is weakened after the introduction of cobalt indicating the presence of Co leads to a long-range disordered structure of interlayer arrangement.

The chemical structures of CN, 0.1CoO/CN, and 0.1Co/CN were also studied by the FT-IR spectroscopy, and the results are shown in Fig. S3. The absorption peak at 812 cm^{-1} is the breathing mode of the triazine units [37]. The absorption band of 1200–1700 cm^{-1} is a characteristic stretch vibration of an aromatic C-N heterocycle [38]. The broad absorption band 3000–3300 cm^{-1} can be attributed to N–H or O–H bonds [39]. There was no significant difference in the FT-IR spectra of 0.1CoO/CN and 0.1Co/CN samples compared to pure CN. The pore structure and surface area of the photocatalysts were determined by the N_2 adsorption and desorption process. As shown in Fig. S4, the CN, 0.1CoO/CN and 0.1Co/CN can be classified as IV isotherm and H3 hysteresis loop, which proves that there are mesoporous structures in the photocatalysts [40,41]. The specific surface areas of CN, 0.1CoO/CN and 0.1Co/CN are 29.35 m^2 g^{-1}, 37.88 m^2 g^{-1} and 44.31 m^2 g^{-1}, respectively. Comparison of the three samples suggests that the presence of cobalt species increases the specific surface area. The large specific surface area is beneficial for exposing more active sites and may make the catalyst exhibit better photocatalytic activity [42].

The morphologies of 0.1CoO/CN pretreated with H_2 at different temperatures and Co/CN samples with different cobalt contents were characterized by scanning-transmission electron microscopy (STEM). The HAADF image and EDS mapping of 0.1CoO/CN sample are shown in Fig. 3. As can be seen in the HAADF image of Fig. 3(a) and the HRTEM image in Fig. S5 (a), no small nanoparticles can be observed in

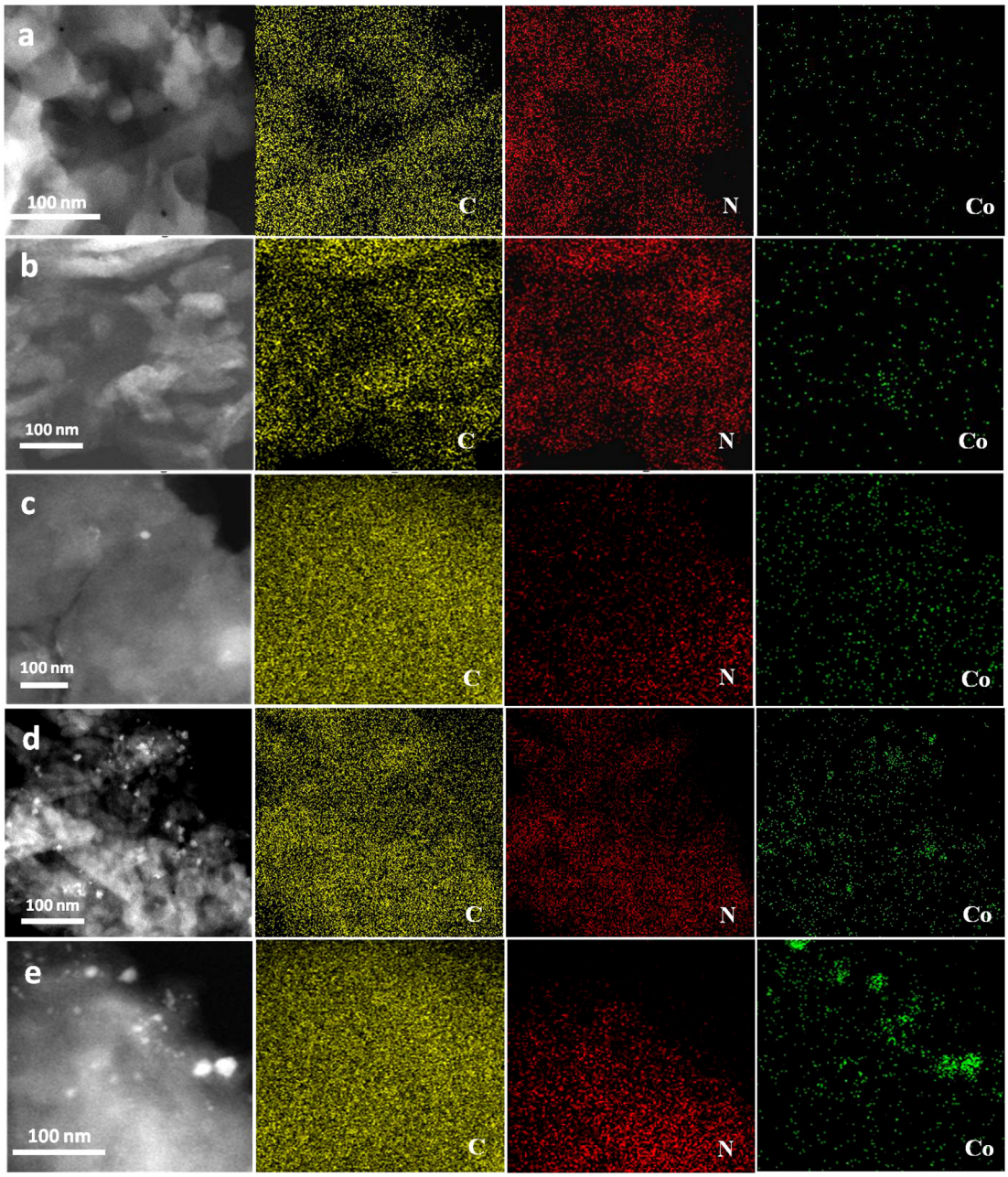

Fig. 3. High-angle annular dark field (HAADF) images and energy dispersive spectrometer (EDS) mappings of 0.1CoO/CN pretreated with H_2 at different temperatures (a) without pretreating, (b) pretreated at 300 °C, (c) pretreated at 350 °C, (d) pretreated at 400 °C and (e) pretreated at 450 °C.

the 0.1CoO/CN sample, which suggests that cobalt species are highly dispersed. The EDS mapping of cobalt element also suggests its high dispersed state. The morphologies of samples pretreated at 300 °C and 350 °C are similar to that of the unpretreated sample, and no particulate cobalt species can be observed, as shown in Fig. 3(b) and Fig. 3(c). However, many small nanoparticles appear when the H_2 pretreating temperature is raised to 400 °C, as shown in Fig. 3(d). When the pretreated temperature increases to 450 °C, the size of the particle grows larger (Fig. 3(e)). The results suggest the dispersion of cobalt species is closely related to H_2-pretreated temperature. For the sample pretreated by H_2 at 400 °C, Fig. S5(b) shows that the lattice fringes of cobalt species agree with the (1 1 1) plane of metallic cobalt, suggesting the appearance of metallic cobalt nanoparticle on the surface of CN. It is known that the formation of small metal cobalt benefits the charge transfer from CN to metal Co [32], and it will facilitate electron-hole separation and improve photocatalytic activity. In addition, the reduction temperature determines the formation and the size of metallic cobalt nanoparticles. Thus, there could be an optimum balance that CoO was reduced to metallic Co effectively by H_2, but without promoting much nanoparticle growth, which shows the best photocatalytic activity.

Fig. 4 shows the HAADF images of Co/CN samples with different cobalt contents, which are produced by H_2-pretreating at 400 °C. Co content of the different Co/CN samples was determined by ICP analysis. As shown in Table 1, the content of cobalt species increases with the amount of cobalt salt precursor used. The size distribution of nanoparticle cobalt is displayed in Fig. 5. From Fig. 4 and Fig. 5, it can be observed that the size of the particle increases with the amounts of cobalt species. As seen in Fig. 4(a) and Fig. 4(b), the particle size increases a little when the amount of cobalt is increased from 0.01Co/CN to 0.05Co/CN. The average diameters of the particles in 0.01Co/CN and 0.05Co/CN samples are (2.5 ± 0.7) nm and (2.7 ± 0.9) nm (Fig. 5(a)

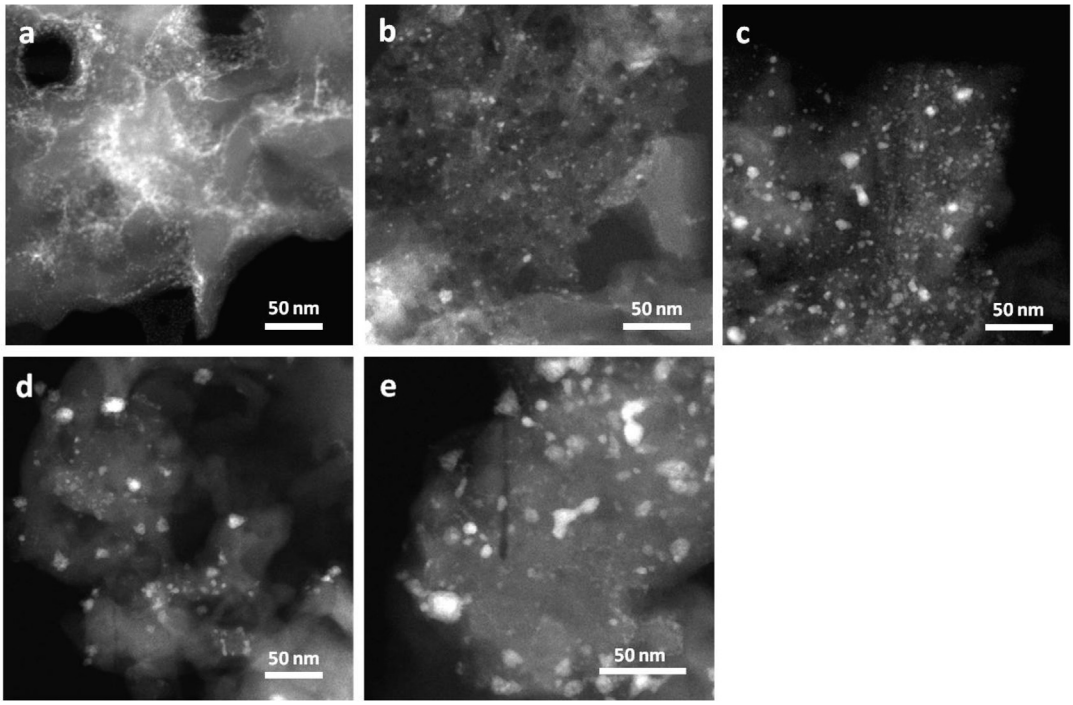

Fig. 4. High-angle annular dark field (HAADF) images of (a) 0.01Co/CN, (b) 0.05Co/CN, (c) 0.1Co/CN, (d) 0.15Co/CN and (e) 0.2Co/CN catalysts.

Table 1
The ICP analysis of Co/CN samples with different Co contents.

Sample	Co contents in Co/CN
0.01Co/CN	0.0163%
0.05Co/CN	0.1903%
0.1Co/CN	0.6843%
0.15Co/CN	0.8180%
0.2Co/CN	0.9380%

and Fig. 5(b)), respectively. For the 0.1Co/CN sample (Fig. 4(c)), the average diameter increases to (3.6 ± 2.2) nm, as shown in Fig. 5(c). The average diameters of 0.15Co/CN and 0.2Co/CN samples become much bigger (Fig. 4(d) and Fig. 4 (e)), and they are (8.3 ± 2.6) nm and (9.0 ± 3.4) nm (Fig. 5(d) and Fig. 5(e)), respectively. Correlating the particle size distribution with the photocatalytic H_2 evolution rate, it can be concluded that the activity of the photocatalyst is closely related to the size of cobalt particle, which further determines the dispersion of exposed cobalt atoms of the catalyst. When the content of cobalt species is lower than the 0.1Co/CN sample, the exposed cobalt atom increases with the amount of cobalt species. Thus, in this region, the photocatalytic activity of catalyst increases with the amount of cobalt species. When the content of cobalt species is higher than the 0.1Co/CN sample, the size of the Co nanoparticle becomes larger, and the exposed cobalt sites may decrease due to the excessive aggregation of cobalt nanoparticles. Thus, in this region, the photocatalytic activity of catalysts decreases with the amounts of cobalt species increasing.

The chemical composition and chemical state of 0.1Co/CN were studied by X-ray photoelectron spectroscopy. Fig. 6(a) shows that two distinct C 1s peaks appear at 284.6 eV and 288.2 eV, respectively. The peak at 284.6 eV corresponds to the C–C bond from carbon conductive tape [43,44], and another peak at 288.2 eV is ascribed to the sp^2 hybrid carbon (C═N−C) of g-C_3N_4 [45,46]. The N 1s spectrum is shown in Fig. 6(b) and can be divided into four peaks at 398.6 eV, 400.2 eV, 401.3 eV and 404.4 eV, which are assigned to sp^2 hybrid N atom in C═N−C, N-$(C)_3$, N–H bond and π-excitation, respectively [47–49]. Fig. 6(c) shows the Co 2p spectrum, which can be fitted to six peaks. The two distinct peaks at 778.5 eV and 793.7 eV are assigned to the $2p_{3/2}$ and $2p_{1/2}$ peak of metallic Co, respectively. The other two peaks are at 780.6 eV and 796.0 eV are attributed to the $Co2p_{3/2}$ and $Co2p_{1/2}$ of Co^{2+}, and the peaks at 786.0 eV and 802.0 eV are ascribed to the satellite peaks of Co^{2+} [50–52]. The presence of Co^{2+} may be attributed to surface reoxidation of metallic Co nanoparticle when the 0.1Co/CN sample was exposed to air. The XPS spectra of 0.1CoO/CN catalyst are shown in Fig. S2. The XPS C 1s and N 1s peaks of 0.1CoO/CN are similar to those of 0.1Co/CN. However, the peak of Co 2p is different. The cobalt species mainly exist as Co^{2+} in the 0.1CoO/CN sample. In addition, as shown in Table 2, the surface atomic ratio of Co in 0.1CoO/CN sample is obviously lower than that in 0.1Co/CN sample, suggesting many Co^{2+} exist in the body phase of carbon nitride in the 0.1CoO/CN sample.

3.3. Optical and electrochemical properties of CN, 0.1CoO/CN and 0.1Co/CN catalysts

The optical absorption of the CN, 0.1CoO/CN and 0.1Co/CN catalysts was studied by UV–vis spectroscopy. As show in Fig. 7(a), the light absorption of pure CN expands from ultraviolet to the visible region. The absorption edge wavelength is 456 nm corresponding to a band gap of 2.72 eV. After the introduction of cobalt species, the absorption edge of 0.1CoO/CN shifts to 468 nm, indicating a red shift of the light adsorption. The HAADF image and EDS mapping in Fig. 3(a) display that the Co species is highly dispersed in 0.1CoO/CN sample. Accordingly, the red shift of the absorption edge for 0.1CoO/CN can be interpreted as indicating the Co doping into the CN lattice. In order to further prove the Co doping, the 0.1CoO/CN sample was boiled with aqua regia for 30 min (denoted as 0.1CoO/CN-A). Then, the UV–vis diffuse reflectance spectrum was again recorded, and the results are displayed in Fig. S6. As can be seen, the UV–vis spectra of 0.1CoO/CN and 0.1CoO/CN-A almost overlap each other. The results suggest the Co atoms have embedded into the lattice structure of CN, which cannot be removed by aqua regia causing the red shift of the absorption edge. Furthermore, it is interesting that the absorption edge of the catalyst becomes further red shifted to 490 nm after H_2 pretreatment. The results suggest the band gap of 0.1Co/CN catalyst is narrower than 0.1CoO/CN catalyst.

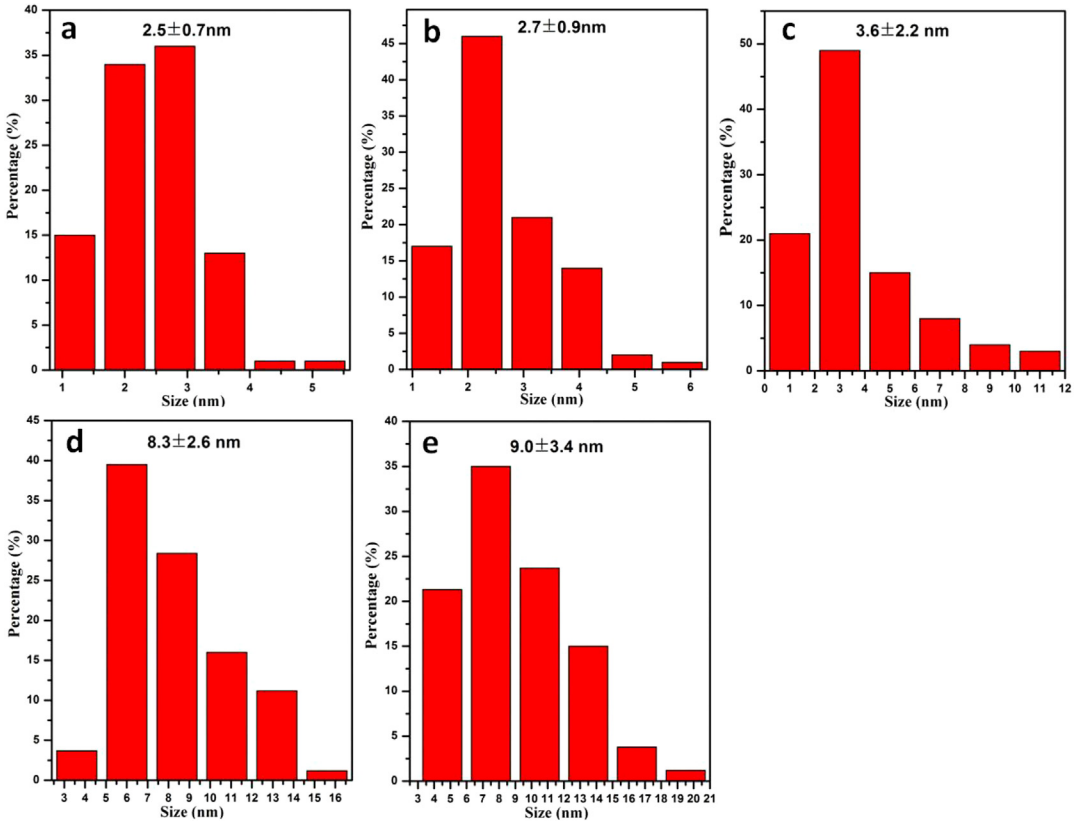

Fig. 5. Size distribution of (a) 0.01Co/CN, (b) 0.05Co/CN, (c) 0.1Co/CN, (d) 0.15Co/CN and (e) 0.2Co/CN catalysts.

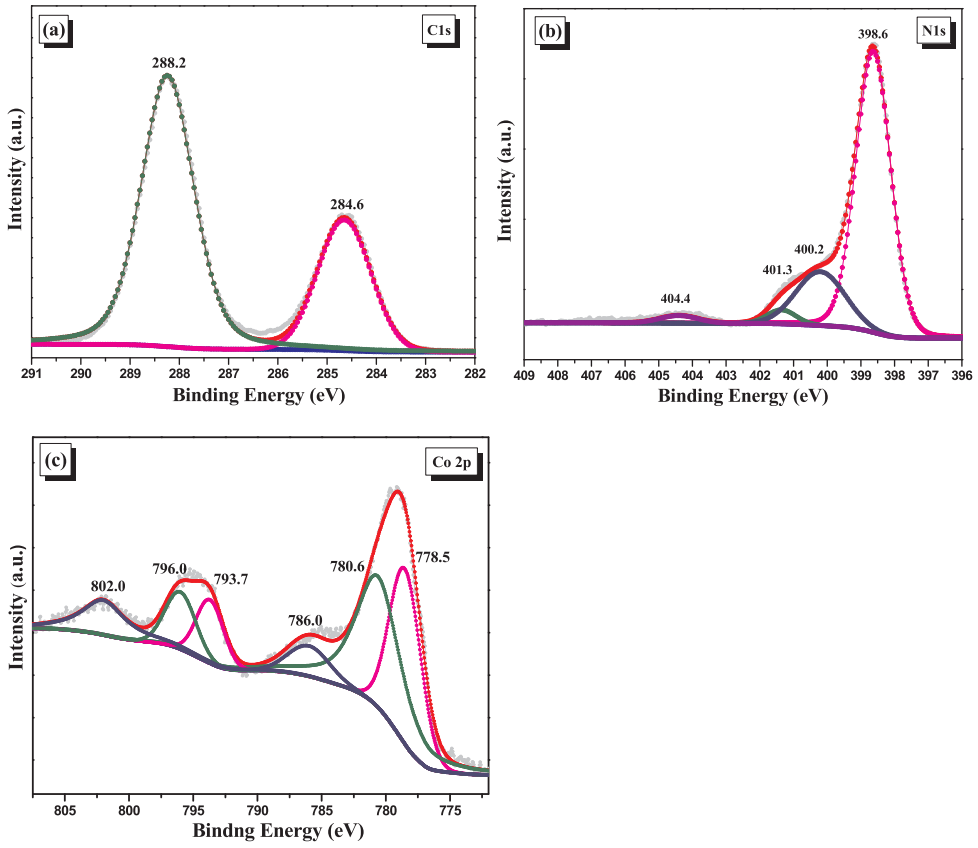

Fig. 6. XPS peaks for (a) C 1s, (b) N 1s and (c) Co 2p of 0.1Co/CN sample.

Table 2
Atomic ratios of the elements determined from the XPS spectra.

Sample	C (%)	N (%)	Co (%)	N/C
0.1CoO/CN	41.40	58.25	0.35	1.41
0.1Co/CN	53.37	46.07	0.56	0.86

Fig. 7(b) shows the Kubelka-Munk function vs. the energy of the absorbed light. As can be seen, the eigen band-gap energies of CN, 0.1CoO/CN and 0.1Co/CN are 2.72 eV, 2.65 eV and 2.53 eV, respectively. These data imply the change of structure or chemical composition of the semiconductor. It is worthy to note that metallic Co has been reported as a catalyst for hydrogenation of nitro compounds [53]. Here, it is proposed that the nitrogen atoms also may be hydrogenated due to catalyzing by metallic Co in the thermal H_2 treatment. Ammonia and other volatile N compounds may form during this process, which make the N atoms leave from the lattice of g-C_3N_4. Consequently, nitrogen-deficient graphitic carbon nitride may be produced. The atomic ratios of 0.1CoO/CN and 0.1Co/CN samples derived from the XPS spectra preliminarily proved our proposal. As can be seen in Table 2, after pretreated by H_2, the ratio of N/C decreases from 1.41 to 0.86. In order to further prove the N vacancy, the EPR spectroscopy was employed to provide support to the generation of N vacancies. The 0.1Co/CN catalyst was first pretreated by aqua regia to remove the metallic Co. The CN and 0.1CoO/CN catalysts were also submitted to the same pretreatment for comparison. The three samples pretreated by acid are denoted as CN-A, 0.1CoO/CN-A and 0.1Co/CN-A, respectively. As shown in Fig. 8, the EPR spectrum of 0.1Co/CN-A shows a strong symmetrical signal centered at g = 2.0033, suggesting the appearance of carbon-based radicals [54]. The results suggest the formation of nitrogen-deficient graphitic carbon nitride. This N-deficient structure could be stable due to the redistribution of the extra electrons in nearest

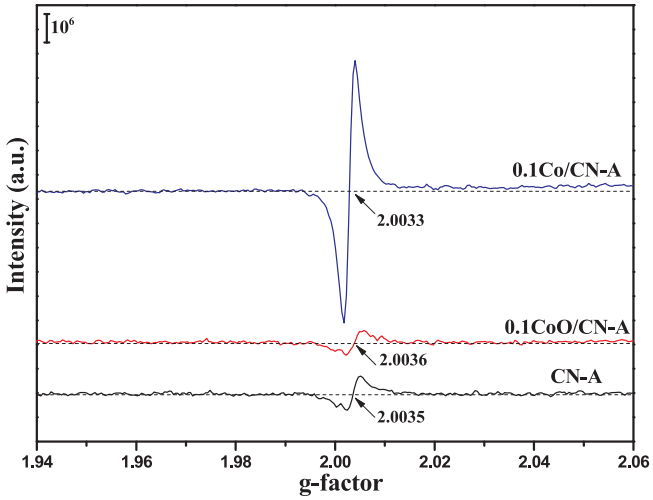

Fig. 8. EPR spectra of CN-A, 0.1CoO/CN-A and 0.1Co/CN-A recorded at room temperature.

carbon atoms through the delocalized p-conjugated bonds of g-C_3N_4 [54]. The CN-A and 0.1CoO/CN-A samples also show a weak similar response for g-C_3N_4. The weak signal recorded for CN-A and 0.1CoO/CN-A indicating that some nitrogen defects can be generated during the thermal polymerization process leading to g-C_3N_4 [54]. In addition, pure CN was also pretreated by H_2 and characterized by EPR for comparison, as shown in Fig. S7. As can be seen here, nearly no difference can be observed between the H_2 pretreated and unpretreated samples, which further supports the role of cobalt promoting N deficiency. XPS analysis was also employed to get more information about the generation of N deficiency. As shown in Fig. S8, compared with

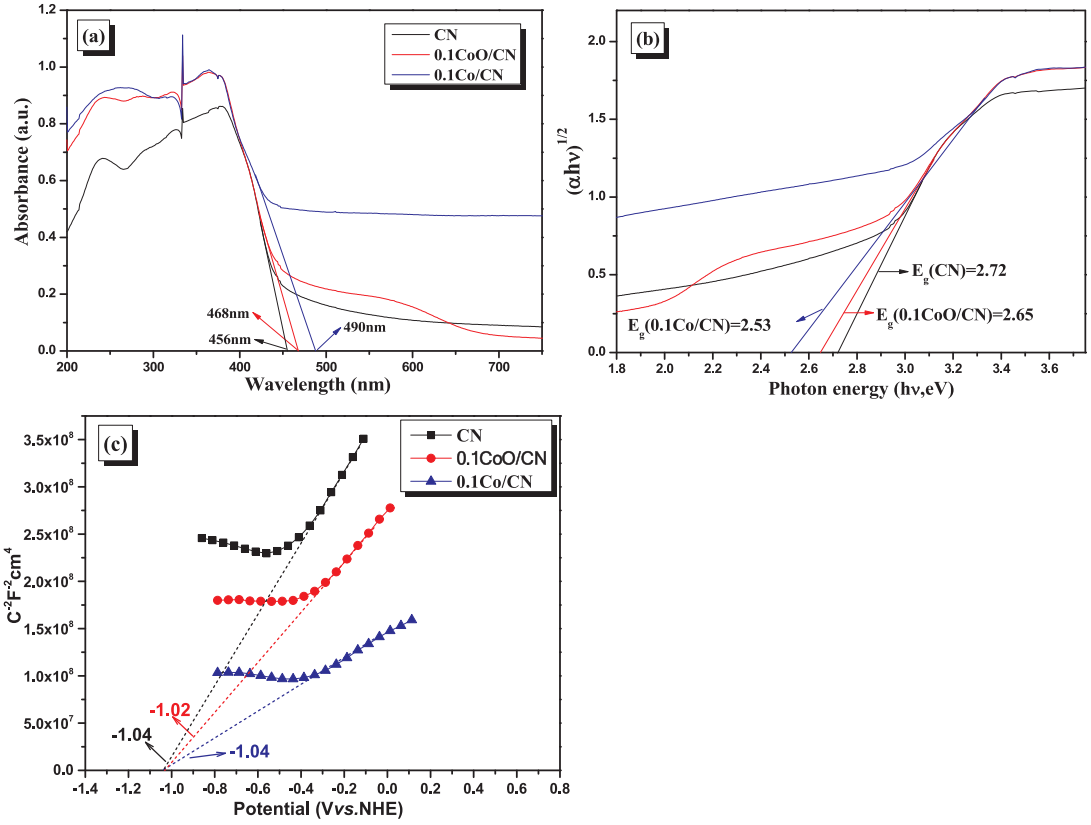

Fig. 7. (a) UV–vis diffuse reflectance spectra, (b) Plots of $(\sigma h\upsilon)^{1/2}$ vs. photon energy ($h\upsilon$) and (c) Electrochemical Mott-Schottky plots of CN, 0.1CoO/CN and 0.1Co/CN samples at pH = 7.

pure CN, the binding energy of N1s of 0.1Co/CN-A sample shifts toward high electron voltage, indicating the redistribution of extra electrons left by the missed nitrogen atoms [55]. The result is agreement with the EPR results well and further prove the existence of N deficiency. Considering the change in the band gap upon doping and reduction of cobalt species, it was interesting to determine the conduction band (CB) and valence band (VB) energy. This study was performed using the Mott-Schottky plots. The Fig. 7(c) gives the Mott-Schottky plots of CN, 0.1CoO/CN and 0.1Co/CN samples with an alternating current potential frequency of 1 KHz. Furthermore, Mott-Schottky plots were also recorded at different frequencies to confirm the tested flat-band potential, as shown in Fig. S9. The (CB) flat-band potentials of the three samples are almost the same, which are approximate −1.04 V, −1.02 V and −1.04 V (vs. NHE), respectively. According to the equation of $E_g = E_{VB} - E_{CB}$, the VB potential of the three catalysts are calculated to be 1.68 V (CN), 1.63 V (0.1CoO/CN) and 1.49 V (0.1Co/CN) vs. NHE. The results reveal that the CB potentials of the photocatalysts are almost unchanged and the VB potentials shift up due to Co doping and generation of N vacancies that make the band gap of the photocatalysts narrow.

DFT calculations were performed to further rationalize the effect of Co doping and N-deficiency on the electronic structure of CN. The structural models used in the calculations are shown in Fig. 9. Fig. 9(a) shows the model of pure CN, and Fig. 9(b) represents the model for 0.1CoO/CN where Co atoms have doped CN lattice. Fig. 9(c) gives the model of Co doped CN with N-deficiency representing the 0.1Co/CN sample. The energy difference between the highest occupied molecular orbital (HOMO) and the lowest unoccupied molecular orbital (LUMO) was calculated. The band gaps between HOMO and LUMO are calculated to be 0.14 a.u. (CN), 0.1 a.u. (Co doped CN) and 0.05 a.u. (Co doped CN with N deficiency). The results indicate the band gap will be narrowed after Co and N-deficiency, which is accordance with the results in experiment (Fig. 7(a) and Fig. 7(b)) and the literatures [56,57]. The calculated results suggest that the values of LUMO in Fig. 9(b) and Fig. 9(c) are almost unchanged compared with that in Fig. 9(a). However, the HOMO shows upward shift when the Co embeds into the central hollow site of CN [34,58]. After the N vacancy forms, the HOMO shows further upward shift. The variation tendency of HOMO is in agreement with the experimental results calculated from Fig. 7(b) and Fig. 7(c), which suggests Co atoms doping into CN lattice and the formation of N vacancy are reasonable.

Fig. 10(a) shows the photoluminescence (PL) spectrum of CN, 0.1CoO/CN and 0.1Co/CN to study the relative charge separation efficiency of these materials. It can be clearly seen that all the spectra of photocatalysts have distinct emission bands in the range of 450 nm ~ 470 nm and show the same emission tendency, but the peak intensities are different. The lower PL intensity indicates the lower efficiency of electron-hole pairs recombination [59,60]. The peak intensities of 0.1CoO/CN and 0.1Co/CN are weaker than that of CN, and 0.1Co/CN being the weakest. The time-resolved fluorescence spectra (TRPL) were conducted to analyze the principle of photogenerated electron transfer and action in the photocatalytic water splitting, as shown in Fig. 10(b). The decay plots of these samples are fitted using triexponential function, and the three lifetimes and corresponding percentage of charge carriers are listed in Table 3. The radiative lifetime (τ_1) is related to the recombination of photogenerated electron and hole. The radiative lifetime (τ_1) follows the order of CN < 0.1CoO/CN < 0.1Co/CN, and the percentage of charge carriers demonstrates the opposite order. The 0.1Co/CN presents the lowest recombination rate of charge carriers, and the metallic Co nanoparticles loaded on the surface of the CN accelerate the photoelectron separation from CN to metallic Co. The τ_2 and τ_3 reflect the lifetimes of non-radiative step and energy transfer process, which are caused by the relaxation effect of a portion of the photogenerated charge carriers. τ_2 and τ_3 of 0.1Co/CN sample are significantly longer than that of the CN and 0.1CoO/CN samples, and the percentage of charge carriers is also significantly higher. The increased percentage and the prolonged lifetime imply the increased possibilities of photogenerated charge carriers participating in the photocatalytic reaction process, which further confirms the effect of metallic Co nanoparticles. PL and TRPL measurement is compatible with the interpretation that the presence of metal Co inhibits the recombination of electron-hole pairs and promotes charge separation, and thus the photocatalytic activity is improved.

The separation of photogenerated charges and the electron transfer process can be determined by photoelectrochemical experiments. Fig. 11(a) shows the transient photocurrent response of CN, 0.1CoO/CN and 0.1Co/CN under visible light irradiation (λ > 420 nm) in on-and-off-cycle mode. The transient photocurrent response of 0.1CoO/CN catalyst is slightly enhanced compared with that of pure CN. After the photocatalyst is pretreated by H_2, the photocurrent response is enhanced significantly. It can be seen that 0.1Co/CN has the strongest photocurrent response compared to CN and 0.1CoO/CN photocatalysts. The electron transfer process is significantly enhanced due to the formation of metallic Co, and the separation efficiency of photogenerated electron-hole pairs becomes higher [61]. EIS was measured to demonstrate the conductivity of different catalysts. The arc radius of the Nyquist plot reflects the magnitude of the electrode resistance and the surface reaction rate [62]. The smaller the radius of the arc suggests the better separation efficiency of photogenerated electron-hole pairs and the higher the charge transfer efficiency [63]. As shown in Fig. 11(b), the pure CN catalyst shows the largest radius. The 0.1CoO/CN sample exhibits smaller radius of arcuate circle than that of CN, indicating that introduction of Co can accelerate charge transfer of the catalyst. The smallest arc radius among the three photocatalysts was measured for the 0.1Co/CN sample, indicating that the metallic Co nanoparticles can further accelerate the electron transfer process.

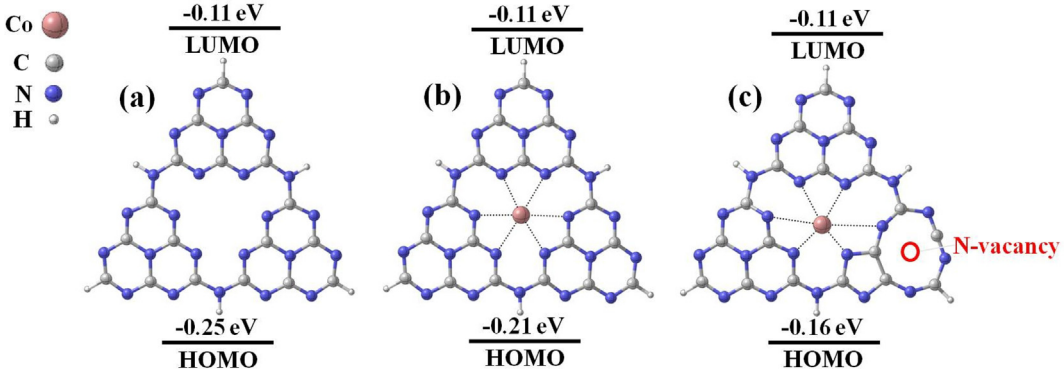

Fig. 9. Structure model of (a) CN, (b) 0.1CoO/CN and (c) 0.1Co/CN samples.

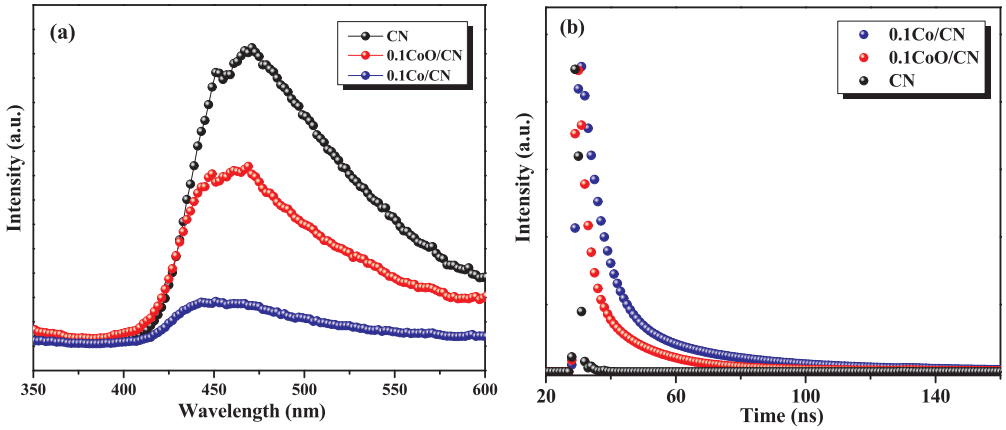

Fig. 10. (a) Photoluminescence spectra and (b) Time-resolved fluorescence spectra (TRPL) of CN, 0.1CoO/CN and 0.1Co/CN samples.

Table 3
The radiative (τ_1), non-radiative (τ_2) and energy transfer process (τ_3) lifetimes of time-resolved fluorescence spectra for CN, 0.1 CoO/CN and 0.1 Co/CN samples.

Sample	τ_1 (ns) (Rel.%)	τ_2 (ns) (Rel.%)	τ_3 (ns) (Rel.%)
CN	0.37 (85)	2.3 (11.8)	3.7 (3.2)
0.1CoO/CN	2.1 (53)	9.5 (28)	20.8 (19)
0.1Co/CN	3.7 (42)	15.3 (35)	30.5 (23)

3.4. Photocatalytic mechanism of H_2 production

The EPR techniques were employed to monitor the free radicals produced in the H_2 evolution reaction to further study the catalytic reaction mechanism. Fig. 12 shows the EPR spectra of CN, 0.1CoO/CN and 0.1Co/CN using POBN as spin trapping agent. Under visible light irradiation, POBN-H· adduct was detected in the three photocatalytic systems [64]. Observation of POBN-H· leads a strong support in favor of H· radical as intermediate in the photocatalytic H_2 generation. However, the rate for H· radicals generation in the three reaction systems is different. As shown in the Fig. 12, after 3 min, weak peaks can be observed in the CN photocatalytic system, and the peak intensity becomes only a little stronger in the 0.1CoO/CN photocatalytic system. However, it should be noted that the peak intensity is significantly enhanced in the 0.1Co/CN photocatalytic system. Therefore, the peak intensities of the three photocatalytic systems follow the order of CN < 0.1CoO/CN < 0.1Co/CN. This order indicates that the metallic Co nanoparticles as cocatalyst speeds the generation rate of H· radicals up, and this effect should lead to an improvement of the photocatalytic hydrogen production. Accordingly, combining the TRPL results, a possible mechanism for visible-light driven H_2 evolution on a metallic Co nanoparticle supported on N-deficient graphitic carbon nitride (g-C_3N_{4-x}) is proposed. Firstly, Co doping and N-deficiency narrow the band gap of photocatalyst, making possible better visible light harvesting. Then, the photogenerated electrons will transfer from the CB of g-C_3N_{4-x} to the metallic Co on the g-C_3N_{4-x}, which should greatly improve the electron-hole separation efficiency. The H^+ from water autohydrolysis can react with the electrons accumulated on the metal Co to form H· radicals more easily, and then H_2 forms finally.

4. Conclusions

A series of Co/CN photocatalysts with different metallic cobalt size supported on N-deficient graphic carbon nitride have been synthesized by H_2 reduction of CoO/CN. The 0.1Co/CN showed the best photocatalytic activity under visible light illumination for H_2 evolution. The photocatalytic activity of 0.1Co/CN was 101.4 times higher than pure CN and 18.0 times higher than 0.1CoO/CN catalyst, respectively. Experimental data indicate that the Co atoms can dope into the g-C_3N_4 lattice, while metallic Co catalyzed hydrogenation generates N vacancies. According to the experimental and computational results, Co doping and N deficiency are responsible for the good utilization of visible light, due to the narrower band gap of photocatalyst. The size of the Co nanoparticle can be tuned by changing the reduction temperature and the cobalt salt precursor amount. The metallic Co accelerates electron transfer rate and charge separation efficiency of photocatalyst. Thus, cobalt species not only disperses on the surface of CN, but also presents as dopant of the CN lattice. For the mechanism study, detection of H· radical suggests that this species is the intermediate in H_2 generation. The metallic Co is beneficial to the generation rate of H·

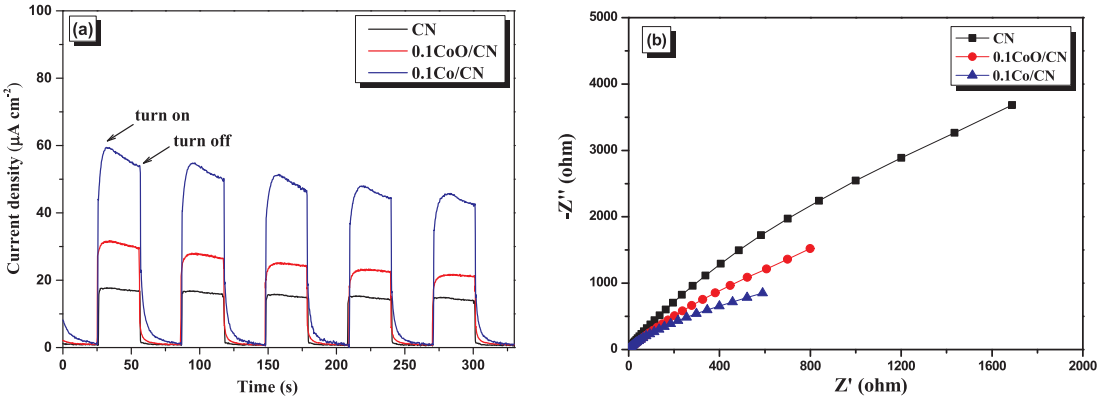

Fig. 11. (a) The transient photocurrent response under visible light irradiation and (b) Electrochemical impedance spectra (EIS) of CN, 0.1CoO/CN and 0.1Co/CN samples.

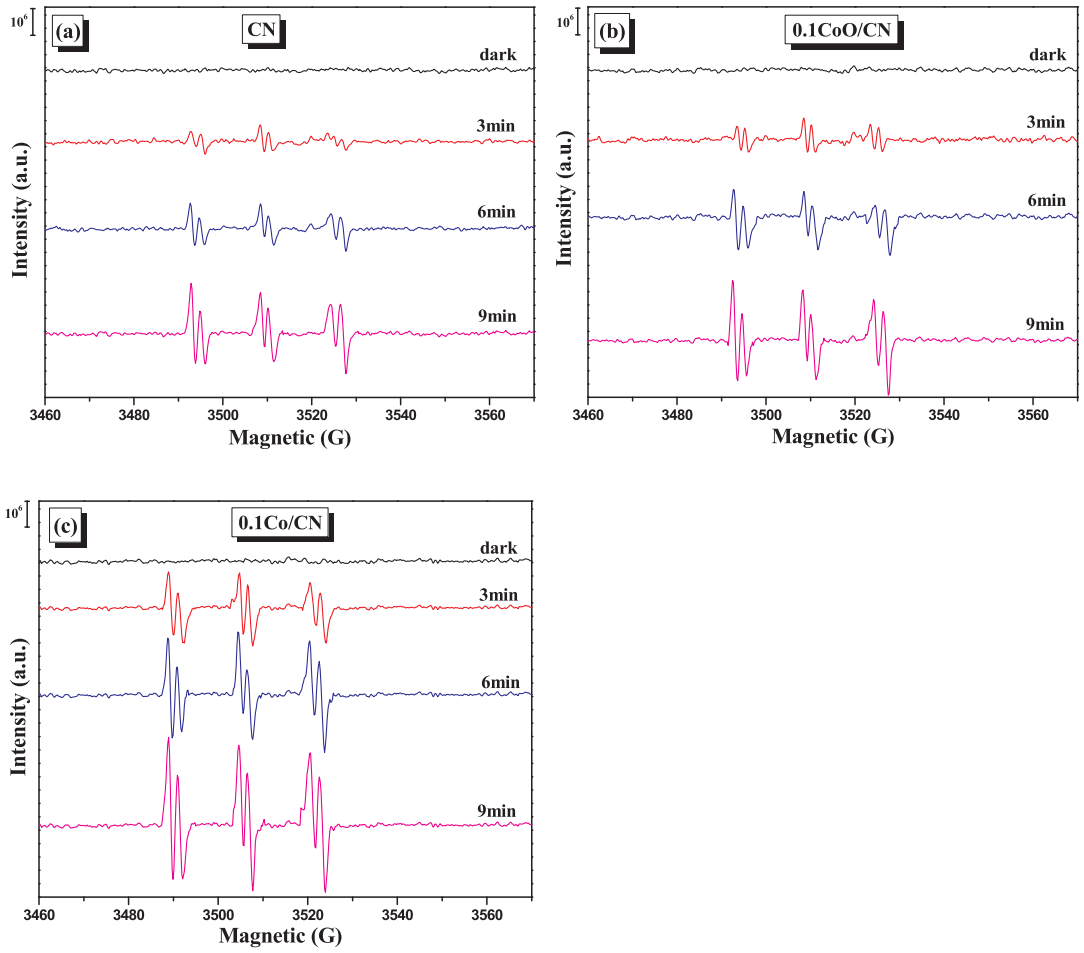

Fig. 12. EPR spectra of H· trapping by POBN (POBN-H·) for (a) CN, (b) 0.1CoO/CN and (c) 0.1Co/CN samples.

radical. Our work can provide a good method for producing and developing non-noble metal photocatalytic materials.

Acknowledgments

This work was supported by the National Natural Science Foundation of China (21976111), Shandong Provincial Natural Science Foundation (ZR2019MB052), and Jinan Program of Science and Technology (201401240).

Appendix A. Supplementary data

Supplementary data to this article can be found online at https://doi.org/10.1016/j.cej.2019.122576.

References

[1] M. Liu, P. Xia, L. Zhang, B. Cheng, J. Yu, Enhanced photocatalytic H_2-production activity of g-C_3N_4 nanosheets via optimal photodeposition of Pt as cocatalyst, ACS Sustain. Chem. Eng. 6 (2018) 10472–10480.
[2] Q. Zhao, J. Sun, S. Li, C. Huang, W. Yao, W. Chen, T. Zeng, Q. Wu, Q. Xu, Single nickel atoms anchored on nitrogen-doped graphene as a highly active cocatalyst for photocatalytic H_2 evolution, ACS Catal. 8 (2018) 11863–11874.
[3] W. Chen, Y. Wang, S. Liu, L. Gao, L. Mao, Z. Fan, W. Shangguan, Z. Jiang, Non-noble metal Cu as a cocatalyst on TiO_2 nanorod for highly efficient photocatalytic hydrogen production, Appl. Surf. Sci. 445 (2018) 527–534.
[4] A. Fujishima, K. Honda, Electrochemical photolysis of water at a semiconductor electrode, Nature 238 (1972) 37–38.
[5] N. Udawatte, M. Lee, J. Kim, D. Lee, Well-defined Au/ZnO nanoparticle composites exhibiting enhanced photocatalytic activities, ACS Appl. Mater. Interfaces 3 (2011) 4531–4538.
[6] H. Zhao, Y. Dong, P. Jiang, G. Wang, H. Miao, R. Wu, L. Kong, J. Zhang, C. Zhang, Light-assisted preparation of a ZnO/CdS nanocomposite for enhanced photocatalytic H_2 evolution: an insight into importance of in situ generated ZnS, ACS Sustain. Chem. Eng. 3 (2015) 969–977.
[7] W. Hung, T. Chien, C. Tseng, Enhanced photocatalytic water splitting by plasmonic TiO_2–Fe_2O_3 cocatalyst under visible light irradiation, J. Phys. Chem. C 118 (2014) 12676–12681.
[8] H. She, Y. Sun, S. Li, J. Huang, L. Wang, G. Zhu, Q. Wang, Synthesis of non-noble metal nickel doped sulfide solid solution for improved photocatalytic performance, Appl. Catal. B: Environ. 245 (2019) 439–447.
[9] E.S.D. Silva, N.M.M. Moura, M.G.P.M.S. Neves, A. Coutinho, M. Prieto, C.G. Silva, J.L. Faria, Novel hybrids of graphitic carbon nitride sensitized with free-base meso-tetrakis(carboxyphenyl) porphyrins for efficient visible light photocatalytic hydrogen production, Appl. Catal. B: Environ. 221 (2018) 56–69.
[10] X. Wang, K. Maeda, A. Thomas, K. Takanabe, G. Xin, J.M. Carlsson, K. Domen, M. Antonietti, A metal-free polymeric photocatalyst for hydrogen production from water under visible light, Nat. Mater. 8 (2009) 76–80.
[11] G. Peng, L. Xing, J. Barrio, M. Volokh, M. Shalom, A general synthesis of porous carbon nitride films with tunable surface area and photophysical properties, Angew. Chem. Int. Ed. 57 (2018) 1186–1192.
[12] S. Cao, J. Low, J. Yu, M. Jaroniec, Polymeric photocatalysts based on graphitic carbon nitride, Adv. Mater. 27 (2015) 2150–2176.
[13] J. Ran, T. Ma, G. Gao, X. Du, S. Qiao, Porous P-doped graphitic carbon nitride nanosheets for synergistically enhanced visible-light photocatalytic H_2 production, Energy Environ. Sci. 8 (2015) 3708–3717.
[14] H. Wang, Y. Bian, J. Hu, L. Dai, Highly crystalline sulfur-doped carbon nitride as photocatalyst for efficient visible-light hydrogen generation, Appl. Catal. B: Environ. 238 (2018) 592–598.
[15] X. Ji, X. Yuan, J. Wu, L. Yu, H. Guo, H. Wang, H. Zhang, D. Yu, Y. Zhao, Tuning the photocatalytic activity of graphitic carbon nitride by plasma-based surface modification, ACS Appl. Mater. Interfaces 9 (2017) 24616–24624.
[16] J. Barrio, M. Shalom, Rational design of carbon nitride materials by supramolecular preorganization of monomers, ChemCatChem 10 (2018) 5573–5586.
[17] Z. Zhou, Y. Zhang, Y. Shen, S. Liu, Y. Zhang, Molecular engineering of polymeric carbon nitride: advancing applications from photocatalysis to biosensing and more, Chem. Soc. Rev. 47 (2018) 2298–2321.
[18] Z. Chen, H. Wang, J. Xu, J. Liu, Surface engineering of carbon nitride electrode by molecular cobalt species and their photoelectrochemical application, Chem. Asian J. 13 (2018) 1539–1543.
[19] J. Barrio, C. Gibaja, J. Tzadikov, M. Shalom, F. Zamora, 2D/2D graphitic carbon

nitride/antimonene heterostructure: structural characterization and application in photocatalysis, Adv. Sustainable Syst. 3 (2019) 1800138.
[20] K. He, J. Xie, Z. Liu, N. Li, X. Chen, J. Hu, X. Li, Multi-functional Ni_3C cocatalyst/g-C_3N_4 nanoheterojunctions for robust photocatalytic H_2 evolution under visible light, J. Mater. Chem. A 6 (2018) 13110–13122.
[21] W. Chen, Y. Wang, W. Shangguan, Metal (oxide) modified (M = Pd, Ag, Au and Cu) $H_2SrTa_2O_7$ for photocatalytic CO_2 reduction with H_2O: the effect of cocatalysts on promoting activity toward CO and H_2 evolution, Int. J. Hydrogen Energy 44 (2019) 4123–4132.
[22] X. Li, W. Bi, L. Zhang, S. Tao, W. Chu, Q. Zhang, Y. Luo, C. Wu, Y. Xie, Single-atom Pt as Co-catalyst for enhanced photocatalytic H_2 evolution, Adv. Mater. 28 (2016) 2427–2431.
[23] Z. Ni, F. Dong, H. Huang, Y. Zhang, New insights into how Pd nanoparticles influence the photocatalytic oxidation and reduction ability of g-C_3N_4 nanosheets, Catal. Sci. Technol. 6 (2016) 6448–6458.
[24] W. Cheng, H. Su, F. Tang, W. Che, Y. Huang, X. Zheng, T. Yao, J. Liu, F. Hu, Y. Jiang, Q. Liu, S. Wei, Synergetic enhancement of plasmonic hot-electron injection in Au cluster-nanoparticle/C_3N_4 for photocatalytic hydrogen evolution, J. Mater. Chem. A 5 (2017) 19649–19655.
[25] J. Yi, X. She, Y. Song, H. Xu, P. Zhang, Z. Mo, L. Liu, D. Du, H. Li, A silver on 2D white-C_3N_4 support photocatalyst for mechanistic insights: synergetic utilization of plasmonic effect for solar hydrogen evolution, RSC Adv. 6 (2016) 112420–112428.
[26] X. Li, J. Yu, M. Jaroniec, X. Chen, Cocatalysts for selective photoreduction of CO_2 into solar fuels, Chem. Rev. 119 (2019) 3962–4179.
[27] L. Liao, Q. Zhang, Z. Su, Z. Zhao, Y. Wang, Y. Li, X. Lu, D. Wei, G. Feng, Q. Yu, X. Cai, J. Zhao, Z. Ren, H. Fang, F. Robles-Hernandez, S. Baldelli, J. Bao, Efficient solar water-splitting using a nanocrystalline CoO photocatalyst, Nat. Nanotechnol. 9 (2014) 69–73.
[28] Z. Li, Y. Wu, G. Lu, Highly efficient hydrogen evolution over $Co(OH)_2$ nanoparticles modified g-C_3N_4 co-sensitized by Eosin Y and Rose Bengal under Visible Light Irradiation, Appl. Catal. B: Environ. 188 (2016) 56–64.
[29] Z. Pan, Y. Zheng, F. Guo, P. Niu, X. Wang, Decorating CoP and Pt nanoparticles on graphitic carbon nitride nanosheets to promote overall water splitting by conjugated polymers, ChemSusChem 10 (2017) 87–90.
[30] F. Guo, W. Shi, H. Wang, M. Han, H. Li, H. Huang, Y. Liu, Z. Kang, Facile fabrication of a CoO/g-C_3N_4 p–n heterojunction with enhanced photocatalytic activity and stability for tetracycline degradation under visible light, Catal. Sci. Technol. 7 (2017) 3325–3331.
[31] W. Chen, Y. Wang, M. Liu, L. Gao, L. Mao, Z. Fan, W. Shangguan, In situ photodeposition of cobalt on CdS nanorod for promoting photocatalytic hydrogen production under visible light irradiation, Appl. Surf. Sci. 444 (2018) 485–490.
[32] N. Zhao, L. Kong, Y. Dong, G. Wang, X. Wu, P. Jiang, Insight into the crucial factors for photochemical deposition of cobalt cocatalysts on g-C_3N_4 photocatalysts, ACS Appl. Mater. Interfaces 10 (2018) 9522–9531.
[33] J. Yu, S. Wang, B. Cheng, Z. Lin, F. Huang, Noble metal-free $Ni(OH)_2$–g-C_3N_4 composite photocatalyst with enhanced visible-light photocatalytic H_2-production activity, Catal. Sci. Technol. 3 (2013) 1782–1789.
[34] C. Sun, H. Zhang, H. Liu, X. Zheng, W. Zou, L. Dong, L. Qi, Enhanced activity of visible-light photocatalytic H_2 evolution of sulfur-doped g-C_3N_4 photocatalyst via nanoparticle metal Ni as cocatalyst, Appl. Catal. B: Environ. 235 (2018) 66–74.
[35] J.S. Kim, J.W. Oh, S.I. Woo, Improvement of the photocatalytic hydrogen production rate of g-C_3N_4 following the elimination of defects on the surface, Catal. Today 293–294 (2017) 8–14.
[36] B. Lin, H. An, X. Yan, T. Zhang, J. Wei, G. Yang, Fish-scale structured g-C_3N_4 nanosheet with unusual spatial electron transfer property for high-efficiency photocatalytic hydrogen evolution, Appl. Catal. B: Environ. 210 (2017) 173–183.
[37] S. Yang, Y. Gong, J. Zhang, L. Zhan, L. Ma, Z. Fang, R. Vajtai, X. Wang, P.M. Ajayan, Exfoliated graphitic carbon nitride nanosheets as efficient catalysts for hydrogen evolution under visible light, Adv. Mater. 25 (2013) 2452–2456.
[38] J. Liu, C. Xiong, S. Jiang, X. Wu, S. Song, Efficient evolution of reactive oxygen species over the coordinated π-delocalization g-C_3N_4 with favorable charge transfer for sustainable pollutant elimination, Appl. Catal. B: Environ. 249 (2019) 282–291.
[39] H. Zhao, Y. Dong, P. Jiang, H. Miao, G. Wang, J. Zhang, In situ light-assisted preparation of MoS_2 on graphitic C_3N_4 nanosheets for enhanced photocatalytic H_2 production from water, J. Mater. Chem. A 3 (2015) 7375–7381.
[40] Y. Zheng, Z. Yu, F. Lin, F. Guo, K.A. Alamry, L.A. Taib, A.M. Asiri, X. Wang, Sulfur-doped carbon nitride polymers for photocatalytic degradation of organic pollutant and reduction of Cr(VI), Molecules 22 (2017) 572.
[41] S. Jiang, C. Xiong, S. Song, B. Cheng, Plasmonic graphene-Like Au/C_3N_4 nanosheets with barrier-free interface for photocatalytically sustainable evolution of active oxygen species, ACS Sustain. Chem. Eng. 7 (2019) 2018–2026.
[42] Z. Mao, J. Chen, Y. Yang, D. Wang, L. Bie, B.D. Fahlman, Novel g-C_3N_4/CoO nanocomposites with significantly enhanced visible-light photocatalytic activity for H_2 evolution, ACS Appl. Mater. Interfaces 9 (2017) 12427–12435.
[43] X. Xu, G. Liu, C. Randorn, J.T.S. Irvine, g-C_3N_4 coated $SrTiO_3$ as an efficient photocatalyst for H_2 production in aqueous solution under visible light irradiation, Int. J. Hydrogen Energy 36 (2011) 13501–13507.
[44] J. Dong, Y. Shi, C. Huang, Q. Wu, T. Zeng, W. Yao, A new and stable Mo-Mo_2C modified g-C_3N_4 photocatalyst for efficient visible light photocatalytic H_2 production, Appl. Catal. B: Environ. 243 (2019) 27–35.
[45] Q. Han, B. Wang, J. Gao, Z. Cheng, Y. Zhao, Z. Zhang, L. Qu, Atomically thin mesoporous nanomesh of graphitic C_3N_4 for high-efficiency photocatalytic hydrogen evolution, ACS Nano 10 (2016) 2745–2751.
[46] R. Shen, J. Xie, X. Lu, X. Chen, X. Li, Bifunctional Cu_3P decorated g-C_3N_4 nanosheets as a highly active and robust visible-light photocatalyst for H_2 production, ACS Sustain. Chem. Eng. 6 (2018) 4026–4036.
[47] H. Huang, K. Xiao, N. Tian, F. Dong, T. Zhang, X. Du, Y. Zhang, Template-free precursor-surface-etching route to porous, thin g-C_3N_4 nanosheets for enhancing photocatalytic reduction and oxidation activity, J. Mater. Chem. A 5 (2017) 17452–17463.
[48] J. Wen, J. Xie, R. Shen, X. Li, X. Luo, H. Zhang, A. Zhang, G. Bi, Markedly enhanced visible-light photocatalytic H_2 generation over g-C_3N_4 nanosheets decorated by robust nickel phosphide ($Ni_{12}P_5$) cocatalysts, Dalton Trans. 46 (2017) 1794–1802.
[49] H. Zhao, S. Sun, P. Jiang, Z. Xu, Graphitic C_3N_4 modified by Ni_2P cocatalyst: An efficient, robust and low cost photocatalyst for visible-light-driven H_2 evolution from water, Chem. Eng. J. 315 (2017) 296–303.
[50] W. Chen, M. Liu, Y. Wang, L. Gao, H. Dang, L. Mao, Non-noble metal Co as active sites on TiO_2 nanorod for promoting photocatalytic H_2 production, Mater. Res. Bull. 116 (2019) 16–21.
[51] J. Zheng, L. Zhang, Incorporation of CoO nanoparticles in 3D marigold flower-like hierarchical architecture $MnCo_2O_4$ for highly boosting solar light photo-oxidation and reduction ability, Appl. Catal. B: Environ. 237 (2018) 1–8.
[52] Z. An, W. Wang, S. Dong, J. He, Well-distributed cobalt-based catalysts derived from layered double hydroxides for efficient selective hydrogenation of 5-hydroxymethyfurfural to 2,5-methylfuran, Catal. Today 319 (2019) 128–138.
[53] L. Liu, P. Concepción, A. Corma, Non-noble metal catalysts for hydrogenation: A facile method for preparing Co nanoparticles covered with thin layered carbon, J. Catal. 340 (2016) 1–9.
[54] Z. Hong, B. Shen, Y. Chen, B. Lin, B. Gao, Enhancement of photocatalytic H_2 evolution over nitrogen-deficient graphitic carbon nitride, J. Mater. Chem. A 1 (2013) 11754–11761.
[55] P. Niu, G. Liu, H. Cheng, Nitrogen vacancy-promoted photocatalytic activity of graphitic carbon nitride, J. Phys. Chem. C 116 (2012) 11013–11018.
[56] J. Bian, L. Xi, J. Li, Z. Xiong, C. Huang, K.M. Lange, J. Tang, M. Shalom, R. Zhang, C = C π bond modified graphitic carbon nitride films for enhanced photoelectrochemical cell performance, Chem. Asian J. 12 (2017) 1005–1012.
[57] J. Barrio, L. Lin, P. Amo-Ochoa, J. Tzadikov, G. Peng, J. Sun, F. Zamora, X. Wang, M. Shalom, Unprecedented centimeter-long carbon nitride needles: synthesis, characterization and applications, Small 14 (2018) 1800633.
[58] M. Zhang, X. Bai, D. Liu, J. Wang, Y. Zhu, Enhanced catalytic activity of potassium-doped graphitic carbon nitride induced by lower valence position, Appl. Catal. B: Environ. 164 (2015) 77–81.
[59] L. Ye, D. Wang, S. Chen, Fabrication and enhanced photoelectrochemical performance of MoS_2/S-Doped g-C_3N_4 heterojunction film, ACS Appl. Mater. Interfaces 8 (2016) 5280–5289.
[60] Y. Dong, L. Kong, P. Jiang, G. Wang, N. Zhao, H. Zhang, B. Tang, A general strategy to fabricate Ni_xP as highly efficient cocatalyst via photoreduction deposition for hydrogen evolution, ACS Sustain. Chem. Eng. 5 (2017) 6845–6853.
[61] S. Guo, Z. Deng, M. Li, B. Jiang, C. Tian, Q. Pan, H. Fu, Phosphorus-doped carbon nitride tubes with a layered micro-nanostructure for enhanced visible-light photocatalytic hydrogen evolution, Angew. Chem. Int. Ed. 55 (2016) 1830–1834.
[62] W. Wu, J. Zhang, W. Fan, Z. Li, L. Wang, X. Li, Y. Wang, R. Wang, J. Zheng, M. Wu, H. Zeng, Remedying defects in carbon nitride to improve both photooxidation and H_2 generation efficiencies, ACS Catal. 6 (2016) 3365–3371.
[63] S. Song, C. Lu, X. Wu, S. Jiang, C. Sun, Z. Le, Strong base g-C_3N_4 with perfect structure for photocatalytically eliminating formaldehyde under visible-light irradiation, Appl. Catal. B: Environ. 227 (2018) 145–152.
[64] X. Bai, L. Wang, R. Zong, Y. Zhu, Photocatalytic activity enhanced via g-C_3N_4 nanoplates to nanorods, J. Phys. Chem. C 117 (2013) 9952–9961.